RSC Advances

This is an *Accepted Manuscript*, which has been through the Royal Society of Chemistry peer review process and has been accepted for publication.

Accepted Manuscripts are published online shortly after acceptance, before technical editing, formatting and proof reading. Using this free service, authors can make their results available to the community, in citable form, before we publish the edited article. This *Accepted Manuscript* will be replaced by the edited, formatted and paginated article as soon as this is available.

You can find more information about *Accepted Manuscripts* in the **Information for Authors**.

Please note that technical editing may introduce minor changes to the text and/or graphics, which may alter content. The journal's standard **Terms & Conditions** and the **Ethical guidelines** still apply. In no event shall the Royal Society of Chemistry be held responsible for any errors or omissions in this *Accepted Manuscript* or any consequences arising from the use of any information it contains.

RSC Advances

ARTICLE

Large-scale synthesis and activation of polygonal carbon nanofibers with thin ribbon-like structures for supercapacitor electrodes

Pingge He,[acd] Lei Liu,[a] Weixin Song,[b] Guoping Xiong,[cd] Timothy S. Fisher,[cd] and Tengfei Chen[*a]

Polygonal carbon nanofibers (PCNFs) were prepared at large scale by chemical vapor deposition using Ni_3Sn_2 intermetallic compound as a catalyst. The PCNFs feature polygonal cross sections with side lengths ranging from 200 nm to 400 nm, as primarily determined by the orthorhombic structure of the Ni_3Sn_2 compound. The PCNFs were subsequently activated by KOH with different concentrations, denoted as a-PCNFs, for supercapacitor electrode applications. The PCNFs were significantly etched during the activation process under a high KOH concentration, forming a unique thin ribbon-like nanostructure with large specific surface area and high content of oxygen-containing functional groups. The electrochemical measurements reveal that a-PCNFs, activated by KOH at a KOH:C weight ratio of 4:1 under 800 ℃, exhibit favorable electrochemical properties with a specific capacitance of 186 F g^{-1} at a current density of 3 A g^{-1} in 1 M Na_2SO_4, good rate capability, low internal resistance, and reasonably stable cycle life. These promising electrochemical properties indicate significant potential for use as scalable supercapacitor electrodes.

Introduction

Electrical double-layer capacitors (EDLCs), an effective and environment-friendly energy storage system, have been the subject of extensive research in recent years because of their high power density, long cycle life, and relatively safe operation.[1-3] Because of their easy accessibility, large specific surface area/porosity and low electrical resistivity, carbon materials are often used as electrodes in EDLCs.[4-7] Carbon nanofibers (CNFs), a one-dimensional carbon nanostructure with high conductivity, physicochemical stability and relatively low cost, have been regarded as attractive candidates for applications in EDLC electrode materials.[8-10] Various methods have been developed to synthesize CNFs[11-13] and among them the chemical vapor deposition (CVD) method, which features hydrocarbon gas as carbon source and metal nanoparticles as catalysts, has been recognized as a preferred method to synthesize CNFs in industry.[14] Transition metal catalysts such as Fe, Co, Ni and their alloys are commonly used during CVD process,[15-17] and the morphologies as well as the microstructures of CNFs are strongly influenced by the chemical and geometric features of catalysts.[18, 19]

Compared with single-element catalysts, bi-metal catalyst systems are efficient for CNF synthesis and play a pivotal role in the formation of CNFs with different shapes and structures.[20,

[21] Bi-metal catalysts such as Fe/Sn,[22] Fe/In[23] and Cu/K[24] have been successfully used to synthesize carbon nanocoils, multi-branched CNFs and other heteromorphic CNF structures. Apart from morphology, the microstructure of CNFs is also affected by bi-metal catalysts. Such a structural diversity of CNFs reflects the anisotropic alignment of graphene layers, which leads to several different types of geometric structures such as platelet, herringbone and tubular CNFs depending on their direction of alignment relative to the fiber axis.[25, 26]

This structural variety makes CNFs versatile in meeting demands of practical applications to some extent. However, CNFs prepared by CVD usually suffer from a relatively low specific surface area, which severely limits their application in supercapacitors.[27] Chemical activation of CNFs with alkali compounds such as KOH or NaOH can significantly improve the capacitance of carbon materials by enlarging specific surface area and generating pores, yet the enlarged specific surface area and porous texture of activated carbons are determined largely by the nature of starting materials.[28] Generally, the CNFs prepared by electrospinning exhibit higher capacitance after activation than that synthesized by CVD,[29] but the relatively high cost and low yield still limits the wide use of electrospinning method in CNFs fabrication. Thus, it is necessary to construct designed architecture of CNFs through CVD process for supercapacitor electrodes.

Herein, CNFs with unique polygonal cross sections were achieved at high yield by a CVD process using Ni_3Sn_2 intermetallic compound as catalyst and ethyne as carbon source. Intermetallic compounds, tending to possess well-defined compositions and crystal structures that differ from their constituent elements,[30] have already been used as catalysts for chemical modification such as hydrogenation and electrochemical oxidation due to their high catalytic efficiency and selectivity.[31] However, few efforts have been made to grow CNFs in the CVD process.

In this work, the intermetallic catalyst compound is found to play a key role in the formation of polygonal CNFs (PCNFs), and the resultant PCNFs were able to be highly activated by KOH. The as-prepared PCNFs and their activated structures (a-PCNFs) were systematically characterized by X-ray diffraction, scanning electron microscopy, transmission electron microscopy, Raman spectrum, X-ray photoelectron spectroscopy and BET characterization, all of which indicate that after KOH activation, the structure of PCNFs significantly changes. By optimizing the KOH:C ratio in the treatment, PCNFs with unique thin-ribbon-like structures were achieved. These a-PCNFs exhibit excellent electrochemical performance in neutral electrolyte with high specific capacitance, good rate capability as well as stable cycle life.

Experimental

Synthesis of PCNFs

All the chemicals were of analytical grade and directly used after purchase without further purification. $Ni(NO_3)_2$ and $SnCl_2$ were chosen as catalyst precursors and the molar ratio of nickel to tin was maintained at 3:2. A urea precipitation process was used to prepare the catalysts. Firstly, $SnCl_2$ was dissolved into 20 mL citric acid (0.01 mol)-ethanol solution, while stirring for 3 h at 60 ^{0}C. The result is called the A solution here. Then, 0.01 mol $Ni(NO_3)_2$ and 0.06 mol urea were simultaneously dissolved into 80 mL deionized water, which is denoted the B solution. Subsequently, A and B solutions were mixed under heating at 120 ^{0}C for 3 h to obtain a hydroxide precipitate. After that, the precipitate was washed, dried and finally calcined at 400 ^{0}C under N_2 atmosphere for 3 h. The as-obtained metal oxide was reduced by H_2 at 450 ^{0}C for 1 h to form catalyst particles. The growth of CNFs was performed in a vertical furnace system using this catalyst at a temperature of 680±5 ^{0}C. During the growth process, reaction gases of C_2H_2 (3.0 L min^{-1}) and H_2 (5.0 L min^{-1}) were introduced into the system at a gas pressure of about 5 kPa.

Chemical activation of PCNFs by KOH

Activation of PCNFs was accomplished through a chemical procedure using KOH as the activating agent. PCNFs and KOH were mixed with KOH:C weight ratios of 2:1, 3:1 and 4:1. The as-obtained samples were carbonized under Ar flow (400 mL min^{-1}) in a vertical furnace (25 cm in diameter), and the reaction temperature was set to 800 ^{0}C with a heating rate of 5 ^{0}C min^{-1}, and a dwell of 1 h at maximum temperature. After the heat treatment, the samples were washed with 5 M HCl solution to remove the mineral impurities and then with distilled water to remove chlorine ions. The activated samples were labelled a-PCNFs-2, a-PCNFs-3 and a-PCNFs-4, corresponding to their KOH:C weight ratios.

Material Characterization

The morphology analyses of products were conducted with a field emission scanning electron microscopy (SEM, Nova Nano 230) and a transmission electron microscopy (TEM, Japan FEM-2100F). The structure of catalysts was characterized by X-ray diffraction (XRD, D/max 2550) combined with the energy dispersive X-ray spectroscopy (EDX) in TEM. Raman spectra were taken with 514.5 nm incident radiation (LabRAM ARAMIS, France HORIBA Jobin Yvon) at a room temperature. X-ray photoelectron spectroscopy (XPS K-Alpha 1063, UK Thermo Fisher) was used to characterize the surface composition of the materials. N_2 adsorption/desorption measurements were performed by using a Quantachrome instrument (Quabrasorb SI-3MP) at 77 K to analyze the porosity of products.

Electrochemical measurements

Electrochemical characterization was conducted on an electrochemical workstation (CHI660C). For capacitance measurements, the working electrode was fabricated by mixing the as-prepared materials with polytetrafluoroethylene at a weight ratio of 1:100, and the mixture was dropped and pressed onto nickel foam (1 cm × 1 cm) under a pressure of 10 MPa. The electrochemical characterization was carried out in a three-electrode configuration in 1 M Na_2SO_4 aqueous solution, with the as-prepared as a working electrode, platinum mesh as a counter electrode, and saturated calomel electrode (SCE) as a reference electrode. Electrochemical impedance spectroscopy (EIS) was conducted using a Modulab (Solartron Analytical) with an amplitude of 5 mV in the frequency ranging from 1 MHz to 1 Hz. All electrochemical tests occurred at room temperature.

Results and discussion

Intermetallic compound Ni_3Sn_2 as catalyst

In order to obtain Ni_3Sn_2 catalysts for CNFs growth, $Ni(NO_3)_2/SnCl_2$ was chosen as the catalyst precursor with a molar ratio of nickel to tin maintained at 3:2. To investigate the structure of catalysts, the as-obtained metal particles were characterized by XRD. The XRD pattern of the catalysts along with the standard XRD pattern of Ni_3Sn_2 is shown in Fig. 1a. The sharp peaks are primarily attributed to the intrinsic diffraction peaks of Ni_3Sn_2 with an orthorhombic structure. The XRD result and TEM-EDX spectrum analysis (see Supporting Information Fig. S1) confirm that the catalyst used in the growth was Ni_3Sn_2 intermetallic compound with an orthorhombic structure. Notably, no carbide formed during the catalytic process, as indicated from the XRD patterns of carbon products after 5 minutes of growth (see Fig. 1b). Consequently, a surface-diffusion catalytic mechanism is proposed to dominate PCNF growth.
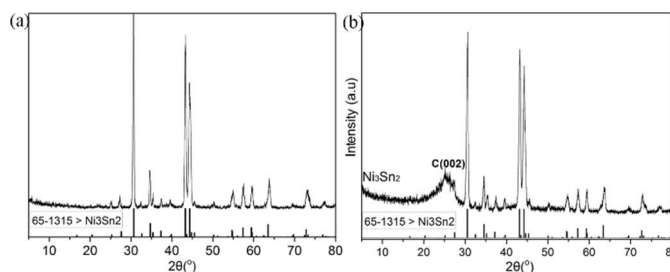

Fig. 1 XRD patterns of (a) catalysts; (b) products after 5 minutes of growth.

Morphology characterization

As shown in Fig. 2a, dense Ni_3Sn_2-catalyzed CNFs were grown in random directions and entangled together. The very high carbon yield (see Supporting Information Fig. S2) confirms the high catalytic efficiency of Ni_3Sn_2 for CNFs growth. The inset of Fig. 2a shows the outline of a fiber with edges generated by two adjacent walls (depicted by the red dotted lines).

However, the CNF structure changed after activation by KOH with different concentrations. At low KOH content (KOH:C = 2:1), the morphology changed little compared to the raw CNFs (see Fig. 2b), while increase of KOH:C weight ratio produced many noticeable grooves on the surface of PCNFs (see Fig. 2c). When the weight ratio increased to 4:1, some fibers were so vigorously activated that their edges were completely etched, leading to open channels in the fiber and many ribbon-like nanosheets (see Fig. 2d).
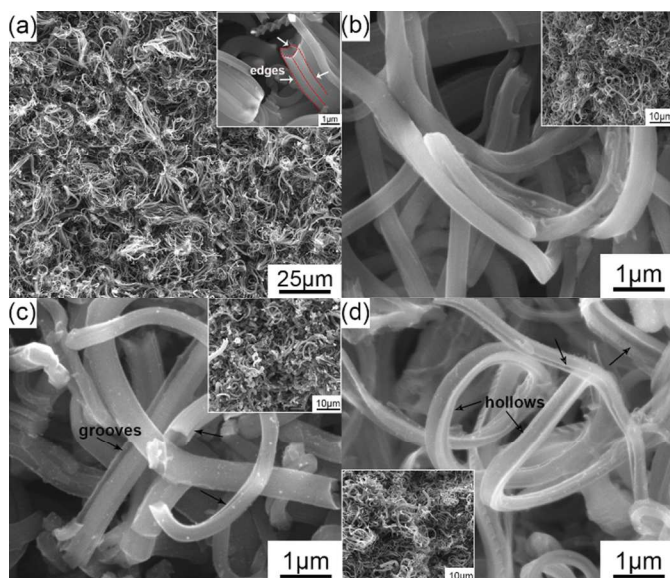

Fig. 2 SEM images of raw CNFs and activated CNFs: (a) raw CNFs (the red dotted line in the inset displays the outline of a fiber); (b) CNFs activated with KOH:C=2:1; (c) CNFs activated with KOH:C=3:1; (d) CNFs activated with KOH:C=4:1.

TEM characterization further elucidates the structural transformation during the activation process. In the TEM image of raw CNFs (see Fig. 3a), stripes distinctly appeared in the border region because of the contrast differences (indicated by arrows) related to the existence of edges. Some edges connected weakly, forming narrow crevices on the surface. Polygonal cross sections formed, as observed in top views of CNFs (see Supporting Information Fig. S3a). Based on the SEM and TEM images, the structure of the as-prepared CNFs is quite different from that of conventional cylindrical CNFs.[32] These PCNFs possess lengths of several microns and feature polygonal cross sections with side lengths ranging from 200 nm to 400 nm. The formation of such PCNFs is highly dependent on the chemical and geometrical characters of Ni_3Sn_2 catalyst, which features a polyhedral structure (confirmed by previous XRD results). Ni has been widely used to grow vertically aligned CNFs,[33] but in this work, with the combination of Sn, which de-wets the graphite nanostructure surfaces and consequently promotes non-linear growth of carbon structures,[34] polygonal CNFs were achieved at large scale.

In contrast, TEM images of a-PCNFs-4 (see Fig. 3b-3c) distinctly display the structural changes after KOH activation.

A large number of PCNFs were significantly etched so that the fiber walls distinctly thinned and the edges were completely broken, consequently forming ribbon-like nanosheets. Notably, after activation, the core as well as the outermost regions of fibers, became ultrathin, indicating such regions were more accessible for KOH etching. After activation, no catalyst particles were observed since the samples were washed with HCl and distilled water several times, consequently removing the metal catalyst particles. More detailed structural characteristics of a-PCNFs-4 are provided in Supporting Information Fig. S3b and S3c.
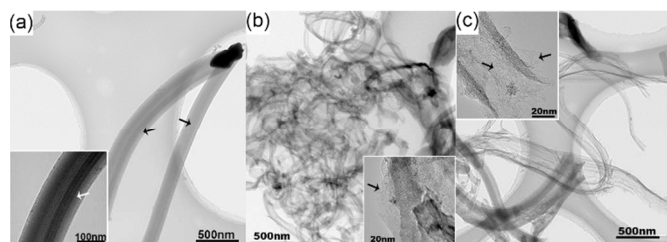

Fig. 3 TEM images of (a) raw PCNFs (arrows indicate contrast differences); (b) and (c) a-PCNFs-4 samples (arrows indicates the ultrathin regions).

Porous structure of activated PCNFs

The nitrogen (N_2) adsorption–desorption isotherms and pore-size distribution curves of the raw PCNFs and a-PCNFs are shown in Fig. 4. Based on the results of Fig. 4a, N_2 adsorption–desorption isotherm of the raw PCNFs is identified as type IV in the IUPAC classification with a typical B-type hysteresis loop, suggesting that mesopores predominate in the raw PCNFs. However, after activation by KOH, the amount of adsorption increased substantially, especially in the range of low pressures, revealing an IUPAC type I isotherm. This difference indicates that activation led to a large increase in the number of micropores. Moreover, the adsorption amount in the BET measurement increased with higher KOH:C weight ratios during the activation process. However, under low pressures, few differences in N_2 adsorption between a-PCNFs-2 and a-PCNFs-3 were observed, showing similar micropore volumes of these two samples. These conclusions are supported by the pore size distribution curves obtained from the N_2 isotherms based on density functional theory (DFT) calculations (see Fig. 4b) that raw PCNFs principally contain mesopores (pore sizes of 3-4 nm) and some micropores (pore size of ≈ 1.5 nm), while a-PCNFs possess primarily micropores with a sizes less than 2 nm.
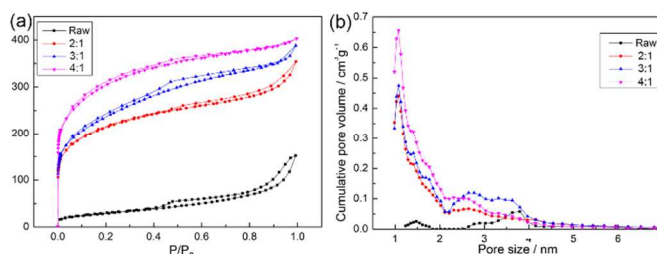

Fig. 4 BET characterization of different samples: (a) N_2 adsorption isotherms and (b) NLDFT pore size distributions of the raw PCNFs and activated PCNFs with different KOH concentrations (KOH:C=2:1, 3:1, 4:1).

The porosity data calculated by the NLDFT method including total specific surface area, total pore volume,

micropore volume, mesopore volume and mesopore specific surface area for all samples are summarized in Table 1. After KOH activation, the total specific surface area and pore volume both increase, and these increases are primarily attributed to micropores.

Table 1 Structural properties of raw and activated PCNFs calculated on the basis of nitrogen absorption data.

Sample	S_{BET} (m^2 g^{-1})	V_t (cm^3 g^{-1})	V_{mi} (cm^3 g^{-1})	V_{me} (cm^3 g^{-1})	S_{me} (m^2 g^{-1})
Raw-PCNFs	106.5	0.235	0.024	0.211	66.6
a-PCNFs-2	717	0.548	0.227	0.227	109.6
a-PCNFs-3	770	0.60	0.348	0.252	158.3
a-PCNFs-4	958.4	0.624	0.471	0.153	104.5

S_{BET}: BET specific surface area; V_t: total pore volume; V_{mi}: micropore volume; V_{me}: mesopore volume; S_{me}: mesopore specific surface area.

Raman spectrum and XPS analysis

Fig. 5a shows the comparative Raman spectra of raw PCNFs and activated PCNFs treated by different KOH concentrations. The Raman spectra of all samples display both wide peaks around 1340 cm^{-1} (denoted as the D peak resulting from disordered carbon) and 1590 cm^{-1} (denoted as the G peak originating from graphitic structure), suggesting that these samples possess highly amorphous structures. The calculated intensity ratios (I_D/I_G) of raw PCNFs, a-PCNFs-2, a-PCNFs-3 and a-PCNFs-4 were 0.93, 1.21, 1.24 and 1.29, respectively. Therefore, the activation process had introduced some structural defects to PCNFs. Nevertheless, the intensity ratio I_D/I_G remained nearly constant for different KOH concentrations in the treatment. The following formula can be used to correlate these Raman ratios to structure:[35]

$$I_D/I_G = C/L \quad (1)$$

where C is 4.4 nm for a laser excitation of 514.5 nm, and L represents the length of crystalline graphite area. Based on the foregoing data, the L values of raw PCNFs and a-PCNFs were calculated to be 4.7 nm and 3.5 nm, respectively, demonstrating that KOH activation damages the original graphite structure of fibers and enlarges the amorphous content.

XPS was employed to investigate the chemical composition of the activated PCNF surface. For comparison, untreated raw PCNFs and a-PCNFs-4 were chosen for the analysis. The C 1s spectrum of raw PCNFs in Fig. 5b clearly indicates a preponderance of carbon atoms in C–C nonfunctional graphitic structures (B.E. = 284.8 ± 0.2 eV), approaching 95 at%. Few C-O functional groups (B.E. = 286.5 ±0.4 eV) existed on fiber surface because of the adsorption of oxygen or water from the air. However, after activation by KOH, hetero-carbon components such as phenolic, alcohol, ether groups (B.E. = 286.5 ±0.4 eV) and carbonyl or quinone groups (B.E. = 287.5 ± 0.2 eV) appeared, amounting to 24.1 at% (see Fig. 5c). The O spectrum of a-PCNFs-4 additionally demonstrates the presence of oxygen-containing functional groups on fiber surfaces (Fig. 5d), and among these, C-O groups account for 87.5 at%, with C=O groups at 12.5 at%. These XPS results indicate that the KOH activation generates many oxygen-containing functional groups on the PCNF fiber surface that would contribute to large electrochemical pseudocapacitance in such electrodes.
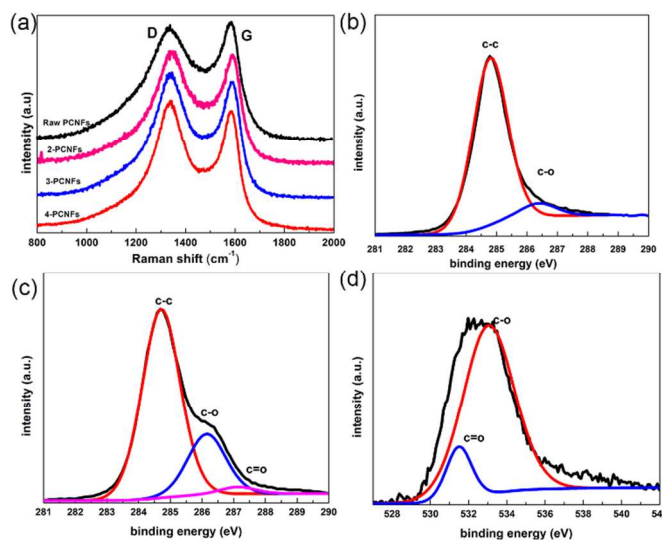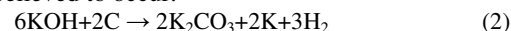

Fig. 5 (a) Raman spectra of the raw and activated PCNFs; (b) XPS C 1s spectrum of raw PCNFs; (c) XPS C 1s spectrum of a-PCNFs-4 and (d) XPS O 1s spectrum of a-PCNFs-4.

Mechanism of KOH activation on PCNFs

During the KOH activation process, the following reaction is generally believed to occur:[36]

$$6KOH+2C \rightarrow 2K_2CO_3+2K+3H_2 \quad (2)$$

At high temperatures, the as-formed K_2CO_3 significantly decomposes to K_2O and CO_2. Moreover, the resulting CO_2 is further reduced by carbon to CO, and K compounds (K_2O and K_2CO_3) are reduced by carbon to metallic K as well.[37, 38] Thus, at 800 °C, the carbon is consumed and finally transforms into carbon monoxide. In this work, the carbon retention rates calculated by the weight ratio of CNFs after and before activation were 0.91, 0.83 and 0.72 for the KOH:C weight ratios of 2, 3 and 4, thus indicating that the degree of activation increases with the KOH:C weight ratio.

Much literature has reported that the morphology of carbon materials changes little upon KOH activation.[27, 39] However, in this work, the structure and morphology of PCNFs significantly changes with activation. As discussed in previous sections, PCNFs appear to grow based on a surface-diffusion mechanism during CVD. In such a process, most carbon atoms gather on

the surface, leading to an inhomogeneous structure with a densely compact shell and a loose core, making the core of PCNFs easily accessible to KOH and thus facilitating the preferential chemical etching at the core. Moreover, some crevices and grooves existing on edges also offer channels for KOH access. Therefore, KOH etching can initiate from the core where carbon atoms are sparse, as well as defects on surface edges (e.g., cracks, crevices, and grooves), and this etching gradually thins the fibers into a porous network. Subsequently, the gases generated during the reaction positively contribute to the development of etching area and porosity both from the core and the surface edges. With higher KOH concentration during the activation process, the etching of PCNFs is even more pronounced, ultimately forming thin ribbon-like structures. The suggested activation process is depicted in Fig. 6.
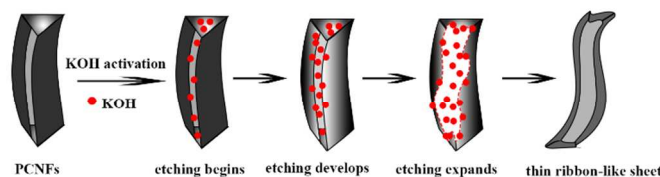

Fig. 6 Schematic of KOH activation of PCNFs.

Electrochemical properties of activated PCNFs

To investigate the electrochemical properties of the activated PCNFs, electrochemical measurements were carried out in a three-electrode system with a neutral electrolyte. The electrochemical performance of a-PCNFs is presented in Fig. 7 including cyclic voltammetry (CV), galvanostatic charge–discharge, EIS, and cycling stability.

Fig. 7a contains comparative CV curves of raw PCNFs and a-PCNFs at a scan rate of 100 mV s^{-1} in a working potential window of 0-1 V vs. SCE. The CV curve of raw PCNFs exhibits a good rectangular shape and no obvious redox peaks, signifying that the capacitance of raw PCNFs mainly originates from electrostatic charge accumulated at the electrode/electrolyte interface (i.e., double-layer capacitance). Nevertheless, strong redox peaks appear in the CV curves of activated samples, indicating pseudocapacitive behavior of the electrode materials. As reported in prior work, the oxidation/reduction of hydroquinone/quinone groups can significantly contribute to pseudocapacitance of carbon-based electrodes.[40-42] More recently, Sliwak et al. proposed that hydroxyl groups can as well play a crucial role in increased pseudocapacitance. Also, high C=O and C-OH group concentrations on CNF electrode surfaces has been shown to increase capacitance in both acid and alkaline media.[43] In this work, the pseudocapacitance of activated PCNFs is mainly attributed to the existence of oxygen-containing functional groups on the fiber surface introduced by KOH activation. Additionally, with increased KOH concentration in the treatment, the redox peaks become more pronounced, and the area of CV curves becomes larger as well, corresponding to larger specific capacitance. Thus, the order of the specific capacitance of PCNF-based electrodes can be deduced as: a-PCNFs-4 > a-PCNFs-3 > a-PCNFs-2> raw PCNFs.

The specific capacitance of these electrodes can be calculated from the galvanostatic charge-discharge curve (see Supporting information Fig. S4) using the following:

$$C_m = (I \times \Delta t) / (\Delta V \times m) \qquad (3)$$

where C_m (F g^{-1}) is the specific capacitance, I (A) is the current, Δt (s) is the discharging time, ΔV (V) is the potential drop during discharge, and m (g) is the mass of active materials. At a current density of 3 A g^{-1}, the specific capacitance of electrodes derived from raw PCNFs, a-PCNFs-2, a-PCNFs-3 and a-PCNFs-4 were calculated to be 27.3, 103, 126, and 187 F g^{-1}, respectively, demonstrating the activation process resulted in large pseudocapacitance that is consistent with results from CV measurements. The specific capacitance of a-PCNFs-4 is much higher than that of other activated CNF-based electrodes in neutral electrolyte and even comparable to that tested in KOH or H$_2$SO$_4$ electrolyte.[27, 44]

Fig. 7b contains CV curves from the a-PCNFs-4 sample operated at a potential between 0-1 V vs. SCE at different scan rates. With increasing scan rates, the redox peaks remain present, and the potential difference between peaks does not broaden, revealing good capacitive performance of the a-PCNFs-4 sample even at high scan rates. The current response to the applied sweep rates is shown in the Supporting Information Fig. S5, in which the peak current is shown to be proportional to the scan rate, indicating that the redox reaction is controlled by surface adsorption.[45]
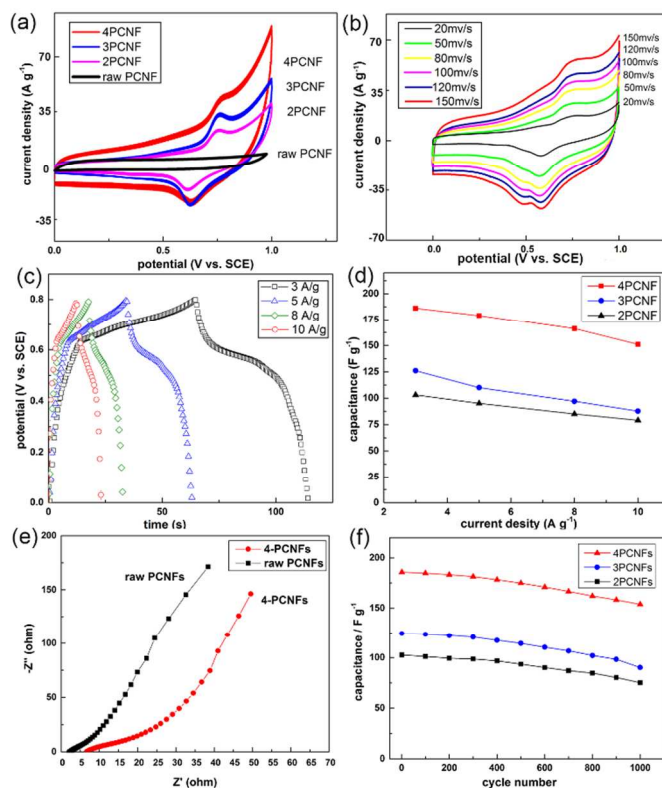

Fig. 7 (a) CV curves of different PCNF-based electrodes at a scan rate of 100 mV/s; (b) CV curves of a-PCNFs-4 electrode at different scan rates; (c) galvanostatic charge/discharge curves of a-PCNFs-4 electrode at different current densities; (d) comparison of the specific capacitances of PCNF electrodes activated with different KOH concentrations at various current densities; (e) Nyquist plots of raw PNCFs and a-PCNFs-4 electrodes; (f) comparison of the cycling performances of PCNF electrodes activated by different KOH concentrations at a current density of 3 A g^{-1}.

In Fig. 7c, the galvanostatic charge-discharge curves of a-PCNFs-4 at different current densities reveal that clear voltage plateaus exist at low currents, suggesting a high

pseudocapacitive contribution to the overall capacitance. However, with increased current density, the voltage plateau narrows and almost disappears at 10 A g^{-1}, which in turn explains the decrease in specific capacitances at high current densities. Fig. 7d summarizes the specific capacitances of PCNFs activated by different KOH concentrations at various current densities. The specific capacitances of all electrodes experience a mild drop with increased current densities. The capacitance of a-PCNFs-4 decreases from 187 F g^{-1} at 3 A g^{-1} to 153.2 F g^{-1} at 10 A g^{-1}, with a capacitance retention of 81.9%.

EIS was performed using a three-electrode system in 1 M Na$_2$SO$_4$ to further evaluate the electrochemical performance, and the Nyquist plots of the raw PCNFs and a-PCNFs-4 electrodes in the frequency range (100 kHz~1 Hz) are displayed in Fig. 7e. In the high frequency region, the real axis intercept represents the internal resistance, including the sum of the contact resistance between the active material and current collector, the intrinsic resistance of the active material, and the ionic resistance of the electrolyte, while the semicircle in the middle frequency region corresponds to the charge transfer resistance.[46] In Nyquist plots, both raw PCNFs and a-PCNFs-4 electrodes exhibit a negligible semicircle, indicating a low charge transfer resistance. The real axis intercepts in the Nyquist plots of raw PCNFs and a-PCNFs-4 are 2.2 and 6.7 Ω, respectively. This result indicates that after activation, the internal resistance slightly increases. Since the activation has generated some oxygen-containing functional groups to a-PCNFs, the internal resistance of a-PCNFs is supposed to increase.[47, 48]

An endurance test was conducted in which the samples underwent 1000 galvanostatic charging/discharging cycles at a current density of 3 A g^{-1}. The specific capacitances of activated PCNFs electrodes as a function of cycle numbers are displayed in Fig. 7f. After 1000 cycles, the specific capacitances of the a-PCNFs-2, a-PCNFs-3 and a-PCNFs-4 decrease moderately to 78.1, 98.3 and 158.5 F g^{-1}, with corresponding capacitance retentions of 76.5% 78.1% and 85.3%, respectively. These cycling results are not outstanding but reasonably good for supercapacitors, also indicating an area for further study and improvement.

The electrochemical performance of activated CNFs or CNTs is concluded in Table 2. Based on these data, after activation, the specific capacitance of a-PCNFs prepared in this work is super higher than that of other CNFs prepared by CVD process, even competitive to that prepared by electrospinning method. Compared to ordinary activated-CNFs, the structure of a-PCNFs in this work changes significantly with numerous thin ribbon-like nanostructures after KOH activation. These thin ribbon-like nanosheets contribute to the remarkable increase of specific surface area of a-PCNFs. Additionally, the unique structure of PCNFs makes carbon atoms more accessible for KOH etching, consequently generating a considerable amount of oxygen-containing functional groups to a-PCNFs, further increasing the pseudocapacitance of a-PCNFs based electrodes. All of them lead to the favorable electrochemical properties of a-PCNFs.

Table 2 Comparison of activated CNFs or CNTs for supercapacitor electrodes

Materials	Synthetic methods	Activation methods	Specific capacitance (F g^{-1})	Electrolyte	Ref.
CNF web	electrospinning	Heating steam	120 (1 A g^{-1})	KOH	[49]
CNT	CVD	KOH activation	53.6 (50 mA g^{-1})	KOH	[50]
CNF	CVD	KOH activation	27.5 (2 mA cm^{-1})	Et$_4$ NBF$_4$	[51]
CNF	electrospinning	Heating steam	134 (1 mA cm^{-1})	KOH	[52]
CNF paper	electrospinning	CO$_2$ activation	220 (50 mA g^{-1})	H$_2$SO$_4$	[53]
			190 (50 mA g^{-1})	KOH	
CNF	electrospinning	ZnCl$_2$ activation	140 (5 mV s^{-1})	KOH	[54]
CNF	electrospinning	KOH activation	100 (1 A g^{-1})	H$_2$SO$_4$	[44]
CNF	electrospinning	KOH activation	255 (1 mA cm^{-1})	H$_2$SO$_4$	[29]
			202 (1 mA cm^{-1})	KOH	
PCNF	CVD	KOH activation	187 (3 A g^{-1})	Na$_2$SO$_4$	This work

Conclusions

In summary, carbon nanofibers with polygonal cross sections were fabricated at large scale using the intermetallic compound Ni_3Sn_2 as a catalyst in a CVD process. As-obtained PCNFs exhibit an inhomogeneous shell-core structure with many edges on the surface. These PCNFs with loose cores and weakly connecting edges make some of the carbon easily accessible for KOH etching. After KOH treatment, the structure of a-PCNFs notably changed such that the fiber walls became thin and most edges were etched, generating large grooves on the surface or thin ribbon-like structures for high KOH:C weight ratio treatments. Moreover, the activation led to significant increases in specific surface area, micropores and oxygen-functional groups of a-PCNFs, enabling excellent pseudocapacitive behavior in a neutral electrolyte with a specific capacitance of 186 F g^{-1} at a current density of 3 A g^{-1}, low internal resistance, good rate capability and reasonably favorable cycle stability. Therefore, these good electrochemical properties coupled with the high yield render this material and the related procedures attractive for promising supercapacitor applications.

Acknowledgements

Notes and references

[a] *State Key Laboratory of Powder Metallurgy, Central South University, Changsha 410083, China*

 E-mail: tengfei@csu.edu.cn; Tel: +86073188830067

[b] *Key Laboratory of Resources Chemistry of Nonferrous Metals, Ministry of Education, College of Chemistry and Chemical Engineering, Central South University, Changsha, 410083, China*

[c] *Birck Nanotechnology Center, Purdue University, West Lafayette, IN 47907, USA*

[d] *School of Mechanical Engineering, Purdue University, West Lafayette, IN 47907, USA*

Electronic Supplementary Information (ESI) available: [details of the structures of catalysts and a-PCNFs-4, as well as the electrochemical properties of a-PCNFs-4 are included.]. See DOI: 10.1039/b000000x/

1. C. Liu, F. Li, L. P. Ma and H. M. Cheng, Adv Mater, 2010, 22, E28-62.
2. P. Simon and Y. Gogotsi, Nat Mater, 2008, 7, 845-854.
3. G. Xiong, C. Meng, R. G. Reifenberger, P. P. Irazoqui and T. S. Fisher, Electroanalysis, 2014, 26, 30-51.
4. G. Xiong, C. Meng, R. G. Reifenberger, P. P. Irazoqui and T. S. Fisher, Energy Technol-Ger, 2014, 2, 897-905.
5. L. L. Zhang and X. Zhao, Chemical Society Reviews, 2009, 38, 2520-2531.
6. M. Inagaki, H. Konno and O. Tanaike, J Power Sources, 2010, 195, 7880-7903.
7. G. Xiong, C. Meng, R. G. Reifenberger, P. P. Irazoqui and T. S. Fisher, Adv Energy Mater, 2014, 4, n/a-n/a.
8. H. Niu, J. Zhang, Z. Xie, X. Wang and T. Lin, Carbon, 2011, 49, 2380-2388.
9. C. Ma, Y. Song, J. Shi, D. Zhang, X. Zhai, M. Zhong, Q. Guo and L. Liu, Carbon, 2013, 51, 290-300.
10. J. R. McDonough, J. W. Choi, Y. Yang, F. La Mantia, Y. Zhang and Y. Cui, Applied Physics Letters, 2009, 95, 243109.
11. L. W. Ji, Y. F. Yao, O. Toprakci, Z. Lin, Y. Z. Liang, Q. Shi, A. J. Medford, C. R. Millns and X. W. Zhang, Journal Of Power Sources, 2010, 195, 2050-2056.
12. C. C. Li, X. M. Yin, L. B. Chen, Q. H. Li and T. H. Wang, J Phys Chem C, 2009, 113, 13438-13442.
13. L. I. Nasibulina, T. S. Koltsova, T. Joentakanen, A. G. Nasibulin, O. V. Tolochko, J. E. M. Malm, M. J. Karppinen and E. I. Kauppinen, Carbon, 2010, 48, 4559-4562.
14. G. G. Tibbetts, M. L. Lake, K. L. Strong and B. P. Rice, Composites Science and Technology, 2007, 67, 1709-1718.
15. G. D. Nessim, Nanoscale, 2010, 2, 1306-1323.
16. Z. B. He, J. L. Maurice, A. Gohier, C. S. Lee, D. Pribat and C. S. Cojocaru, Chemistry Of Materials, 2011, 23, 5379-5387.
17. A. Romero, A. Garrido, A. Nieto-Marquez, P. Sanchez, A. de Lucas and J. L. Valverde, Microporous And Mesoporous Materials, 2008, 110, 318-329.
18. I. A. Merkulov, M. Yoon and D. B. Geohegan, Carbon, 2013, 60, 41-45.
19. D. W. Li, L. J. Pan, D. P. Liu and N. S. Yu, Chem Vapor Depos, 2010, 16, 166-169.
20. W.-C. Liu, H.-K. Lin, Y.-L. Chen, C.-Y. Lee and H.-T. Chiu, ACS nano, 2010, 4, 4149-4157.
21. J. Zhang, J.-O. Müller, W. Zheng, D. Wang, D. Su and R. Schlögl, Nano Letters, 2008, 8, 2738-2743.
22. J. Sun, A. A. Koós, F. Dillon, K. Jurkschat, M. R. Castell and N. Grobert, Carbon, 2013, 60, 5-15.
23. W. Wang, K. Yang, J. Gaillard, P. R. Bandaru and A. M. Rao, Advanced Materials, 2008, 20, 179-182.
24. X. Y. Tao, X. B. Zhang, L. Zhang, J. P. Cheng, F. Liu, J. H. Luo, Z. Q. Luo and H. J. Geise, Carbon, 2006, 44, 1425-1428.
25. S.-H. Yoon, S. Lim, S.-h. Hong, W. Qiao, D. D. Whitehurst, I. Mochida, B. An and K. Yokogawa, Carbon, 2005, 43, 1828-1838.
26. I. Martin-Gullon, J. Vera, J. A. Conesa, J. L. González and C. Merino, Carbon, 2006, 44, 1572-1580.
27. V. Barranco, M. A. Lillo-Rodenas, A. Linares-Solano, A. Oya, F. Pico, J. Ibanez, F. Agullo-Rueda, J. M. Amarilla and J. M. Rojo, J Phys Chem C, 2010, 114, 10302-10307.
28. J. A. Maciá-Agulló, B. C. Moore, D. Cazorla-Amorós and A. Linares-Solano, Microporous and Mesoporous Materials, 2007, 101, 397-405.
29. V. Barranco, M. Lillo-Rodenas, A. Linares-Solano, A. Oya, F. Pico, J. Ibañez, F. Agullo-Rueda, J. Amarilla and J. Rojo, The Journal of Physical Chemistry C, 2010, 114, 10302-10307.
30. J. C. Bauer, X. Chen, Q. S. Liu, T. H. Phan and R. E. Schaak, Journal Of Materials Chemistry, 2008, 18, 275-282.

31. A. Ota, M. Armbruster, M. Behrens, D. Rosenthal, M. Friedrich, I. Kasatkin, F. Girgsdies, W. Zhang, R. Wagner and R. Schlogl, J Phys Chem C, 2011, 115, 1368-1374.

32. J. J. Jiang, M. Z. Qu, G. M. Zhou, X. B. Huang and J. Shao, Carbon, 2012, 50, 323-325.

33. A. V. Melechko, V. I. Merkulov, T. E. McKnight, M. Guillorn, K. L. Klein, D. H. Lowndes and M. L. Simpson, Journal of applied physics, 2005, 97, 041301.

34. J. Sun, A. A. Koós, F. Dillon, K. Jurkschat, M. R. Castell and N. Grobert, Carbon, 2013, 60, 5-15.

35. F. Tuinstra and J. L. Koenig, The Journal of Chemical Physics, 1970, 53, 1126-1130.

36. J. Wang and S. Kaskel, J Mater Chem, 2012, 22, 23710-23725.

37. J. C. Wang and S. Kaskel, Journal of Materials Chemistry, 2012, 22, 23710-23725.

38. E. Raymundo-Pinero, P. Azais, T. Cacciaguerra, D. Cazorla-Amoros, A. Linares-Solano and F. Beguin, Carbon, 2005, 43, 786-795.

39. C. Merino, P. Soto, E. Vilaplana-Ortego, J. M. Gomez de Salazar, F. Pico and J. M. Rojo, Carbon, 2005, 43, 551-557.

40. H. A. Andreas and B. E. Conway, Electrochimica acta, 2006, 51, 6510-6520.

41. M.-K. Seo and S.-J. Park, Current Applied Physics, 2010, 10, 241-244.

42. S. Roldán, M. Granda, R. Menéndez, R. Santamaría and C. Blanco, The Journal of Physical Chemistry C, 2011, 115, 17606-17611.

43. A. Śliwak, B. Grzyb, J. Ćwikła and G. Gryglewicz, Carbon, 2013, 64, 324-333.

44. M.-K. Seo and S.-J. Park, Materials Science and Engineering: B, 2009, 164, 106-111.

45. P. Simon, Y. Gogotsi and B. Dunn, Science Magazine, 2014, 343.

46. Z. Fan, J. Yan, T. Wei, L. Zhi, G. Ning, T. Li and F. Wei, Adv Funct Mater, 2011, 21, 2366-2375.

47. A. Pandolfo and A. Hollenkamp, J Power Sources, 2006, 157, 11-27.

48. C.-T. Hsieh and H. Teng, Carbon, 2002, 40, 667-674.

49. C. Kim and K. Yang, Appl Phys Lett, 2003, 83, 1216-1218.

50. B. Xu, F. Wu, Y. Su, G. Cao, S. Chen, Z. Zhou and Y. Yang, Electrochim Acta, 2008, 53, 7730-7735.

51. S.-H. Yoon, S. Lim, Y. Song, Y. Ota, W. Qiao, A. Tanaka and I. Mochida, Carbon, 2004, 42, 1723-1729.

52. C. Kim, K.-S. Yang and W.-J. Lee, Electrochemical and solid-state letters, 2004, 7, A397-A399.

53. E. Ra, E. Raymundo-Piñero, Y. Lee and F. Béguin, Carbon, 2009, 47, 2984-2992.

54. C. Kim, B. T. N. Ngoc, K. S. Yang, M. Kojima, Y. A. Kim, Y. J. Kim, M. Endo and S. C. Yang, Adv Mater, 2007, 19, 2341-2346.

Graphical Abstract
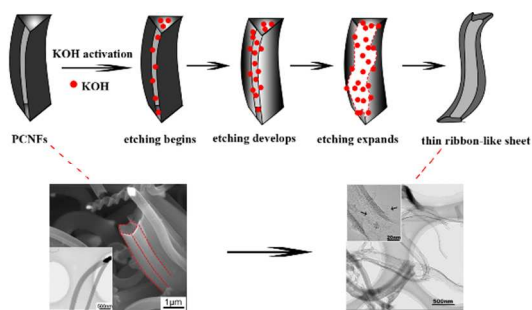
Polygonal carbon nanofibers are activated by KOH with thin ribbon-like nanosheets for application in supercapacitor electrodes, performing favorable electrochemical properties.